Microstructures in a carburized steel after isothermal pearlitic treatment

Mathews, J. Abraham; Farahani, H.; Sietsma, J.; Petrov, R. H.; Mecozzi, M. G.; Santofimia, M. J.

DOI
10.1016/j.jmst.2023.03.017

Publication date
2023

Document Version
Final published version

Published in
Journal of Materials Science and Technology

Journal of Materials Science & Technology 160 (2023) 66–75

Contents lists available at ScienceDirect

Journal of Materials Science & Technology

journal homepage: www.elsevier.com/locate/jmst

Research Article

Microstructures in a carburized steel after isothermal pearlitic treatment

J. Abraham Mathews[a,*], H. Farahani[a,b], J. Sietsma[a], R.H. Petrov[a,c], M.G. Mecozzi[a], M.J. Santofimia[a]

[a] Department of Materials Science and Engineering, Delft University of Technology, Mekelweg 2, 2628 CD, Delft, The Netherlands
[b] Tata Steel Research & Development, IJmuiden, The Netherlands
[c] Department of Electromechanical, Systems and Metal Engineering, Ghent University, Tech Lane Ghent Science park-Campus A Zwijnaarde, Technologiepark 46, Belgium

ARTICLE INFO

Article history:
Received 21 December 2022
Revised 16 February 2023
Accepted 13 March 2023
Available online 18 April 2023

Keywords:
Pearlite formation
Carburized steel
$M_{23}C_6$ carbide
Kinetics
Solute drag

ABSTRACT

The influence of carbon concentration variations on pearlite formation (20 h at 600 °C) in a case-carburized steel is investigated. The resultant microstructure shows three distinct regions: carburized case, a transition region, and the original core. The microstructural transition from the case to the core regions is observed to be relatively sharp. The investigated region of the carburized case (0.9 wt.% C) contains two types of pearlite: ferrite + cementite and ferrite + $M_{23}C_6$, where the pearlitic aggregate with $M_{23}C_6$ shows faster formation kinetics. The kinetics of pearlite formation in the transition region (0.3 wt.% C) is very slow and is observed with only $M_{23}C_6$ carbide. Only around 40% austenite decomposes into pearlite in the transition region, which, in comparison to the carburized case region of 0.9 wt.% C is a fraction that is lower by a factor of two. Pearlite is absent in the investigated core region (0.16 wt.% C). The microstructure in this region is predominantly martensite and pro-eutectoid ferrite, with a fraction of ferrite well below the equilibrium fraction. Ferrite formation in this region is limited by the redistribution of mainly Ni, Mn, and Cr, and their resulting solute drag effect on the austenite/ferrite interface. A thermodynamic and kinetic argumentation of these observations is provided with the help of thermodynamic data, precipitation simulations, and a general mixed-mode Gibbs energy balance model.

1. Introduction

Case carburization is a widely applied heat treatment on steel components that operate in fatigue-prone environments. The carbon diffusion during the carburization process induces a concentration gradient. Appropriate heat treatment of steels with such carbon concentration gradients results in a hard case and a ductile core. Additionally, carburized components are characterized by significant compressive residual stresses at the surface and high fractions of retained austenite in the case regions [1,2,3]. These factors have been reported to enhance the fatigue properties and hence the service life of carburized parts [1,2,4,5].

For large-sized components such as the main-shaft bearings of wind turbines, a martensitic matrix with case depths exceeding 3 mm is required to sustain the high service stresses and to avoid sub-surface microstructural damage. However, carburization treatments to obtain such deep cases require prolonged holding at high temperatures, which often results in coarse austenite grains. Martensite formed from coarse-grained austenite, in comparison to that formed from fine-grained austenite, has been reported to exhibit lower strength and cleavage fracture resistance [6,7]. Furthermore, reduction in rolling contact fatigue life of bearing steels due to coarse prior austenite grains is well documented in literature [8,9,10,11]. Therefore, the conventional post-carburization procedure of quenching followed by tempering is not adequate, in most cases, for components with large case depth requirements.

One of the heat treatment strategies to eliminate the coarse austenite grains formed during the carburization treatment is to apply a subsequent pearlitic treatment before re-austenitization and hardening. The pearlitic microstructure provides a high density of interfaces that act as favorable austenite nucleation sites [12] during the subsequent re-austenitization treatment. This leads to the refinement of austenite, which, on quenching, transforms into a fine martensitic microstructure. This is an alternative grain

* Corresponding author.
E-mail address: J.AbrahamMathews@tudelft.nl (J.A. Mathews).

https://doi.org/10.1016/j.jmst.2023.03.017

Table 1
Nominal composition of the investigated steel (wt.%).

C	Ni	Cr	Mo	Si	Mn	P	S	Fe
0.16	3.3	1.4	0.2	0.4	0.55	0.007	0.003	Bal.

refinement strategy to the bainitic annealing treatment studied by Mathews et al. [13].

In order to achieve optimal properties in carburized components involving several stages, it is important to understand the microstructure development in each of these stages. The current study focuses on the microstructure formed in isothermal pearlitic treatment after carburization. The characterization of microstructure developing in the pearlitic treatment is not only of fundamental interest but also has significant practical implications due to the following reasons:

(1) During re-austenitization, the characteristics of the austenite matrix, developed from the microstructure obtained during the pearlitic treatment, contribute to the final properties of the heat-treated steel. As austenite formation is a structure-sensitive process [14,15], the microstructure from which it forms plays an important role in determining the kinetics, grain size, morphology, and the homogeneity of alloy distribution in austenite.
(2) Due to economic and environmental reasons, it is preferred to apply the shortest carburizing time to achieve the required case depth. This comes with the risk of under-designing with respect to case depth specifications. Under such instances, microstructure analysis of the intermediate stages of heat treatment, like the pearlitic treatment investigated in this study, is useful to ascertain the reliability of the applied carburization process parameters.
(3) For steels that undergo intermediate heat treatments after carburization, the presence of carbon gradients dictates the kinetics of subsequent phase transformations. Since the driving force for phase transformation varies with depth below the carburized surface, different decomposition products of austenite can be obtained along this depth. In the instance of a sharp microstructural transition, the surrounding regions will be subjected to stress concentration. If such sharp microstructural transitions occur within a load-bearing region and are not eliminated in subsequent heat treatment stages, they can have a detrimental impact on the performance of carburized components. Therefore, the microstructure analysis after pearlitic treatment is needed to rectify any unforeseen anomalous microstructure development.

The present work explores the microstructure development during the isothermal pearlitic treatment of a case-carburized steel. Microstructures corresponding to various carbon concentrations in the case, transition, and core regions are experimentally investigated. The rationale behind the experimental observations is elucidated with the help of equilibrium phase calculations, precipitation simulations, and a general mixed-mode Gibbs energy balance (GEB) model [16].

2. Material and experimental methods

The investigated alloy is steel used for large bearings in wind turbines. The chemical composition of the as-received steel is shown in Table 1.

2.1. Heat treatment

The as-received sample was case-carburized, followed by an isothermal pearlitic treatment (IPT), as schematically shown in Fig. 1. A copper stop-off paint was applied on 5 of the 6 sides of the sample prior to the heat treatment to allow carbon diffusion into the required side only. The sides painted with copper will not uptake carbon. This is illustrated in the inset in Fig. 1. Carburization treatment (CT) was carried out employing a boost & diffuse treatment in an atmosphere of endogas and methane for 60 h. In the boost phase, the sample was carburized at a carbon potential (C_p) of 1.2 at 980 °C for 40 h. Thereafter, the temperature was reduced to 970 °C and a lower C_p, 0.8, was applied for the remaining 20 h of the carburization treatment, called the diffuse phase. After the carburization treatment, the sample was transferred into a furnace that was stabilized at 600 °C in a protective N_2 atmosphere, and isothermally treated for 20 h. This treatment is referred to as isothermal pearlitic treatment (IPT), after which the sample was quenched in hot water (60 °C). The estimated time to transfer the carburized sample into the second furnace is 120 s, and the cooling rate from 970 °C to 600 °C is ≈ 0.5 °C/s.

2.2. Specimen sampling

The heat-treated sample was cut using electrical discharge machining to obtain cross- sectional and lateral specimens as schematically shown in Fig. 2. The cross-sectional specimen, of dimensions 8 × 1 × 13 mm^3 ($x \times y \times z$), contains the entire carbon gradient arising from the carburization treatment z-direction. Lateral specimens of dimensions 10 × 3 × 1 mm^3 ($x \times y \times z$) were cut from different depths, 1, 5 and 9 mm from the carburized surface, and were investigated in the x-y plane (plane of uniform carbon content).

2.3. Experimental procedure

Microstructural analyses were made using optical and electron microscopes. Optical microscopy was performed using a Keyence VHX-6000 microscope enabled with a 2D stitching function. Wide-area optical micrographs (OM) were obtained by capturing multiple images of the specimen while moving the specimen via the stage in a serpentine motion. Scanning electron microscopy (SEM) images were captured using a JEOL JSM-6500F field emission gun scanning electron microscope at an accelerating voltage of 15 kV. The specimens for microstructural analyses were metallographically prepared and etched in 5% Nital solution.

Transmission electron microscopy (TEM) was performed on a spherical-aberration corrected FEI Titan microscope operating under 300 kV voltage and equipped with Thermo Scientific Ceta™ 16 M camera for acquiring high-resolution electron transmission microscope (HRTEM) lattice images. Elemental composition maps were obtained from energy dispersive X-ray spectroscopy (EDX) collected for each beam position in a scanning transmission electron microscopy (STEM) image using the super-X ChemiSTEM™ detectors. The crystal structure information was obtained from the resulting Fourier transforms of HREM images and selected area diffraction patterns (SADP). For TEM specimen preparation, the material was mechanically thinned to 20 µm and further prepared to electron transparency using Ar ion milling.

The volume fractions of the phases were determined by X-ray diffraction (XRD) experiments using a Bruker D8-Advance diffractometer. Co Kα radiation was used in the 2θ scan from 35° to 130° with a counting time per step of 2 s and a step size of 0.035° of 2θ. Data evaluation was made using Bruker's DiffracSuite EVA software (version 6.0), Profex/BGMN. The volume fractions of the phases were calculated using Rietveld refinement.

The carbon concentrations at various depths were measured on the cross-sectional specimen using Electron Probe Micro Analyser (EPMA). The measurements were made with a JEOL JXA 8900R microprobe employing wavelength dispersive spectroscopy using an

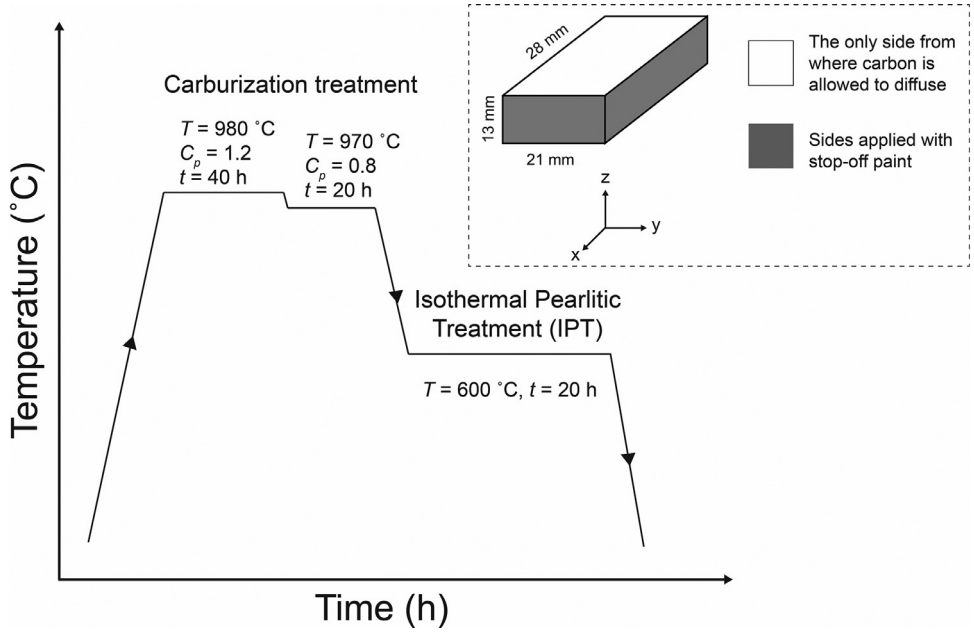

Fig. 1. Schematic representation of the heat treatment applied on the as-received sample. The inset illustrates the sides painted with the copper stop-off paint prior to the heat treatments.

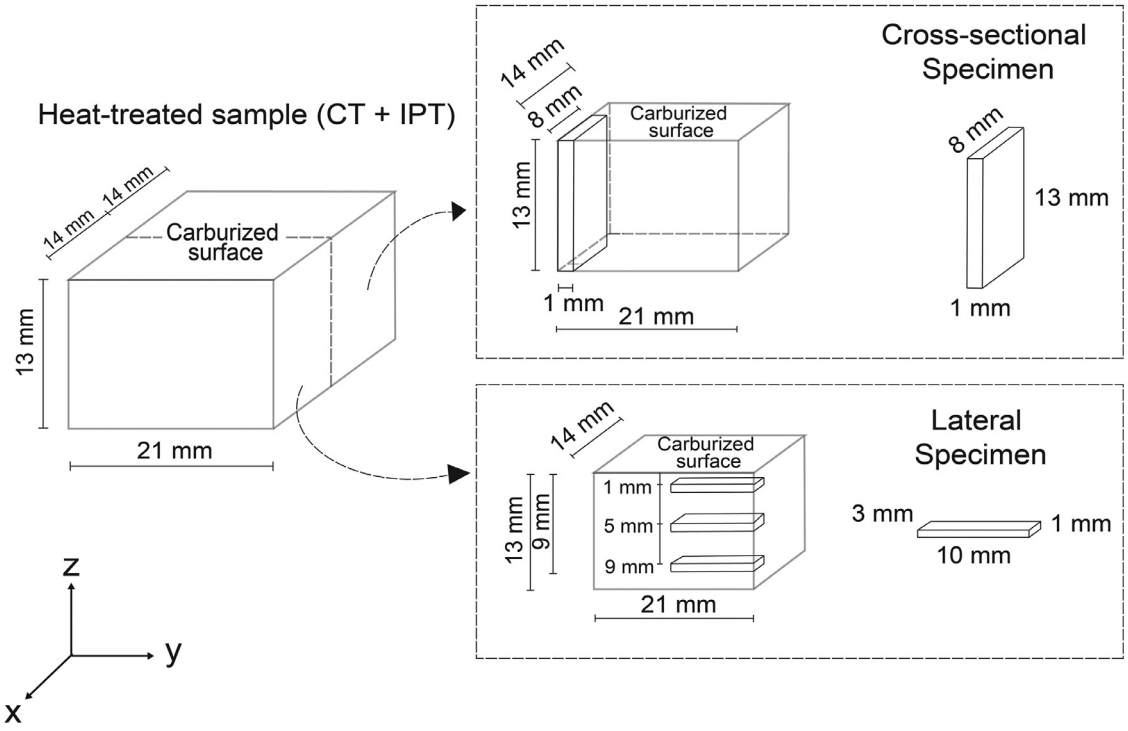

Fig. 2. Schematic of the specimen sampling after the heat treatments.

electron beam energy of 10 keV and a beam current of 100 nA. The carbon concentrations at each depth are quantified from the measurements along a line of 850 µm with points separated by a distance of 5 µm. The composition at the location of analysis was determined using the X-ray intensities of the constituent elements after background correction relative to the corresponding intensities of the reference materials. The intensity ratios thus obtained were processed with a matrix correction program CITZAF [17]. The suppression of the deposition of carbonaceous substances on the sample surface and the removal of surface-adsorbed species that can interfere with the measurement accuracy was ensured by applying an air jet during the measurement. Consequently, a high-precision carbon measurement is made, with a low counting error of 0.02 wt.% for the spectral line of carbon.

Vickers hardness measurements were made on a Dura-scan 70 (Struers) hardness tester applying a load of 9.8 N for a dwell time of 10 s. At least 10 measurements were made to calculate the average hardness.

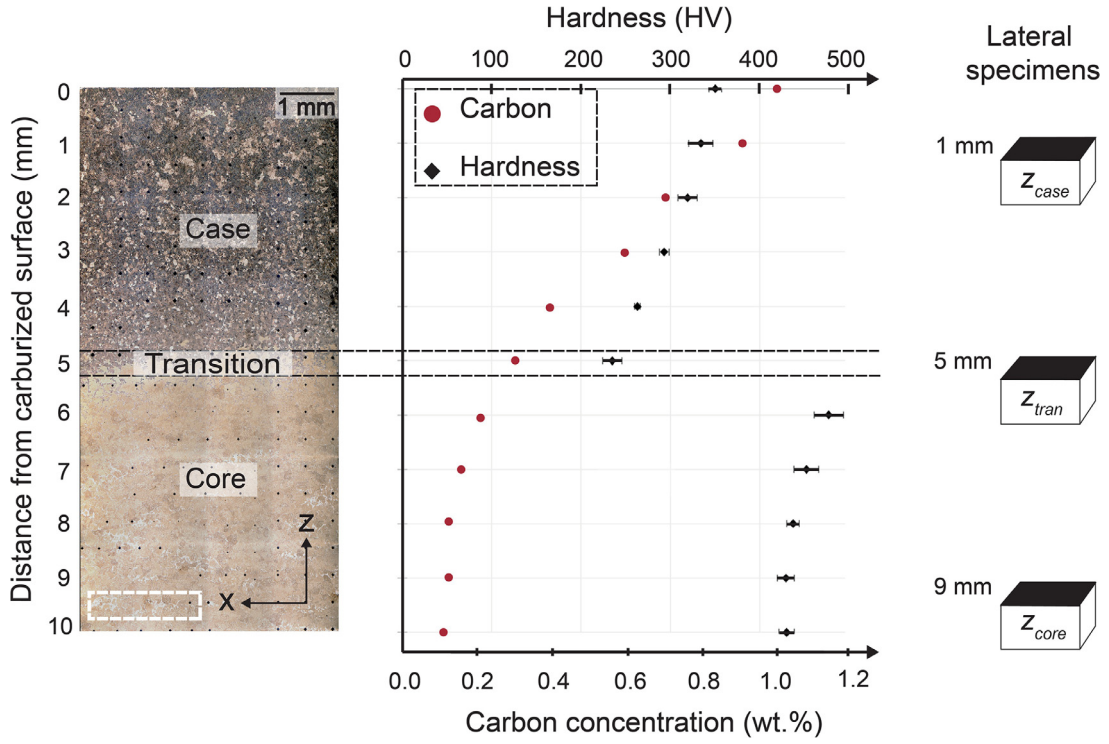

Fig. 3. Microstructural, hardness, and carbon gradients from the case to the core regions after IPT, viewed in the cross-sectional plane. Schematics of the locations of specimens z_{case}, z_{tran}, and z_{core} are also provided. The shaded regions of these lateral specimens represent the plane of investigation.

3. Results

The resulting microstructures vary as a function of carbon concentration from the carburized surface to the bulk. An overview of these microstructures is provided in Section 3.1 by analysing the cross-sectional specimen, followed by the analyses of the microstructures of lateral specimens containing 0.9 wt.% C, 0.3 wt.% C, and 0.16 wt.% C (refer to Fig. 2). These specimens are hereafter called z_{case}, z_{tran}, and z_{core}, respectively. The microstructural analyses of these specimens are provided in Sections 3.2.1, 3.2.2, and 3.2.3, respectively.

3.1. Cross-sectional analysis of the microstructure

Microstructure, hardness, and carbon gradients in the cross-sectional plane after IPT is shown in Fig. 3. Three regions are distinguished: case, transition, and core. Case region is specified in this study, according to the definition in [18], as the region below the carburized surface to the carbon content attaining 0.3 wt.%. Accordingly, the case region extends up to a depth of 5 mm. The carbon concentration in the case, measured by EPMA, ranges from ≈ 1 wt.% to 0.3 wt.%. The case microstructure is pearlitic, and its hardness values are observed to decrease as a function of carbon concentration from 350 ± 8 HV at 1 wt.% C to 235 ± 10 HV at 0.3 wt.% C. The transition region, defined according to the microstructure, is a narrow zone (≈ 0.5 mm) below 5 mm from the carburized surface and has a carbon content of around 0.3 wt.%. The microstructure in this region is a mixture of pearlite and martensite. This region is indicated within the dashed lines in Fig. 3. Its hardness is 235 ± 10 HV. Below the transition region is the core. The carbon concentration in the core varies from ≈ 0.3 wt.% to 0.16 wt.%. The core microstructure is predominantly martensitic with pro-eutectoid ferrite bands (for instance within the rectangle in the micrograph of Fig. 3). The hardness just below the transition region is ≈ 250 HV higher than the transition region. A gradual decrease in hardness is observed within the core region until ≈ 8 mm, below which the carbon concentration and the hardness values do not vary significantly. The high hardness of the core region stems from the martensitic microstructure.

The carbon contents of the lateral specimens used in this study are quantified from the EPMA measurements made on the cross-sectional specimen. A schematic of the specimens z_{case}, z_{tran}, and z_{core} is shown in Fig. 3. The thickness of these specimens is 1 mm, and they are cut from a depth of 1, 5 and 9 mm, respectively, from the carburized surface. It is emphasized that carbon redistribution may occur during the 20 h of isothermal treatment. Assuming a negligible carbon redistribution during the cooling phase from carburization, a preliminary quantification was made using EPMA to compare the carbon gradient shown in Fig. 3 with that of a sample that was carburized and quenched. The results showed that the carbon redistribution was not significant, falling within the experimental errors.

3.2. Microstructural analyses of lateral sections

The analyses and the quantification of the various phases for 0.9 wt.% C, 0.3 wt.% C, and 0.16 wt.% C are performed by investigating the lateral specimens z_{case}, z_{tran}, and z_{core} (dark surfaces indicated in Fig. 3), respectively. The results are discussed in this section.

3.2.1. Specimen z_{case}

The volume fractions of phases present in specimen z_{case} quantified from XRD analysis are 86 ± 1 vol.% of BCC that represents ferrite (α), 8 ± 1 vol.% of $M_{23}C_6$, and 6 ± 1 vol.% of cementite (θ). A comparison of the measured and equilibrium phase fractions (at 600 °C) is shown in Fig. 4(a). The measured frac-

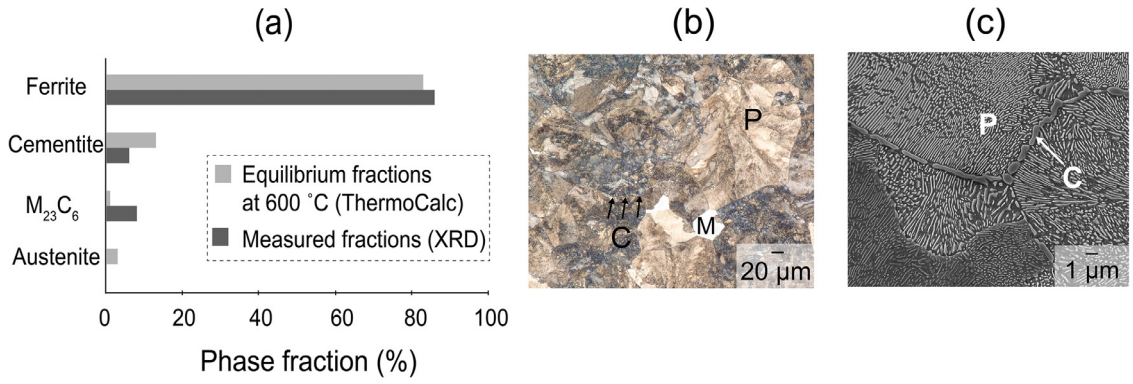

Fig. 4. Microstructural characterization of specimen z_{case}. (a) A comparison of the measured (XRD analysis) and equilibrium phase fractions (using Thermo-Calc at 600 °C). The volume fractions of the phases measured using XRD have an error of ± 1 vol.%. (b) Optical and (c) scanning electron micrographs showing the various microstructural constituents. P: pearlite, M: martensite, and C: carbide.

tions of $M_{23}C_6$ and θ are significantly different from the equilibrium phase fractions calculated using Thermo-Calc: 13% θ and 1% $M_{23}C_6$, in which the equilibrium distribution of metal atoms, 'M', in the sublattice sites are predominantly Fe and Cr. Additionally, Thermo-Calc predicts 3% austenite (γ) at 600 °C. However, FCC peaks that represent γ were not detected in the diffraction analyses. This indicates either its complete absence or a volume fraction below the X-ray detection limit (≈ 1 vol.%). The martensite start temperature (M_s) for the equilibrium composition of γ in specimen z_{case} is 64 °C, predicted from Andrews equation [19]. Therefore, the room-temperature microstructure may contain martensite. However, the peaks of martensite (distinguishable from ferrite because of the tetragonality in the lattice structure due to a high carbon content [13]) were not observed in the XRD patterns.

Microstructure characterization of specimen z_{case} using optical microscopy shows pearlite with a few regions of martensite (1% area). The prior austenite grain boundaries are decorated with carbides. These microstructural constituents are indicated in Fig. 4(b). The morphology of pearlite is shown in Fig. 4(c). Various pearlite colonies with orientation differences in the alternate lamellae of α and carbide can be observed. Although XRD analysis reveals the presence of θ and $M_{23}C_6$ in specimen z_{case}, differentiation between the two types of carbides cannot be made from these microscopy analyses.

The identification of the type of carbides present in pearlite was made using TEM by obtaining the crystal structure information from the selected area diffraction patterns. The carbides present at the prior austenite grain boundaries were characterized by taking the Fast Fourier transforms (FFT) from the high-resolution Transmission Electron Microscope (HRTEM) images. The results, Fig. 5, show that the pearlitic carbide structure of specimen z_{case} is a mixture of θ and $M_{23}C_6$. Both these carbides are also present at the prior austenite grain boundaries. The encircled regions in the TEM micrographs in Fig. 5 (a-d) are the regions from where the crystal structures of the carbides were characterized. Diffraction patterns of the pearlitic carbides from regions 1 (Fig. 5(a)) and 2 (Fig. 5(b)) are shown in Fig. 5(e) and (f), respectively. Inevitably, diffraction patterns of the surrounding matrix were collected at the same time. The reflections marked in yellow are from α-Fe planes and the weak reflections (marked in white) are from the carbide lamellae. From the diffraction analyses, it is inferred that the pearlitic carbide in region 1 has a cubic structure pertaining to $M_{23}C_6$ (zone axis [1 $\bar{1}$ 0]), whereas that from region 2 has an orthorhombic structure pertaining to θ (zone axis [3 $\bar{2}$ 0]). Regions 3 and 4 in Fig. 5(c) and (d) show the carbides that were characterized from the prior austenite grain boundaries. The FFT of HRTEM images from these locations are shown in Fig. 5(g) and (h). The FFT from region 3 fits $M_{23}C_6$ carbide (zone axis [$\bar{9}$ 5 1 2]), whereas that from region 4 fits θ (zone axis [2 0 $\bar{1}$]).

3.2.2. Specimen z_{tran}

The microstructure of specimen z_{tran}, from the transition region (0.3 wt.% C), is a mixture of pearlite and martensite, as shown in Fig. 6(a–c). The area fraction of pearlite was calculated from Fig. 6(a) as 0.4 using image analysis with the software ImageJ. The remaining fraction, which is martensite, does not have a spatial distribution resembling microstructural bands (pearlite-martensite) despite the inherently present chemical segregation bands (width ≈ 400 μm) of Ni, Cr, Mn, Mo, and Si [13]. The prior austenite grain boundaries are devoid of pro-eutectoid products as shown in Fig. 6(b). Pearlite that has grown from the grain boundaries into the grain can be observed, as indicated by the arrow in Fig. 6(b). The SEM micrograph shown in Fig. 6(c) shows the morphology of the pearlite in specimen z_{tran}. The morphology of the carbides is different from those observed in specimen z_{case} (refer to Fig. 4(c)): fragmented, discrete, and having a larger interlamellar spacing. XRD analysis shows 98 (±1) vol.% of BCC and 2 (±1) vol.% of $M_{23}C_6$. Note that a distinction between the pearlitic ferrite (BCC) and martensite (BCT) was not made from the XRD analysis due to the lack of tetragonality in the martensite crystal lattice, which results in ferrite-martensite peaks overlapping. During the Rietveld fitting of the diffraction pattern of specimen z_{tran}, martensite (BCT) was therefore excluded in the determination of the volume fractions. Peaks corresponding to γ-FCC or cementite are not detected, indicating volume fractions below 1 vol.%. From the XRD analysis, it is interpreted that the carbides present in pearlite in specimen z_{tran}, Fig. 6(c), are $M_{23}C_6$.

3.2.3. Specimen z_{core}

The microstructure of specimen z_{core} is predominantly martensite. Ferrite is present at the prior austenite grain boundaries, appearing in the form of non-continuous bands as indicated by arrows in Fig. 7(a). The area fraction of ferrite was calculated from Fig. 7(a) as 7% using ImageJ. The width of ferrite grains is less than ≈ 20 μm, inferred from Fig. 7(b). XRD analysis of specimen z_{core} shows a fully BCC structure with no detectable peaks of γ-FCC, $M_{23}C_6$, or cementite. The tetragonality of martensite in this microstructure, as in specimen z_{tran}, appears to be too low to detect reliably. Hence, martensite peaks are not distinguishable from ferrite.

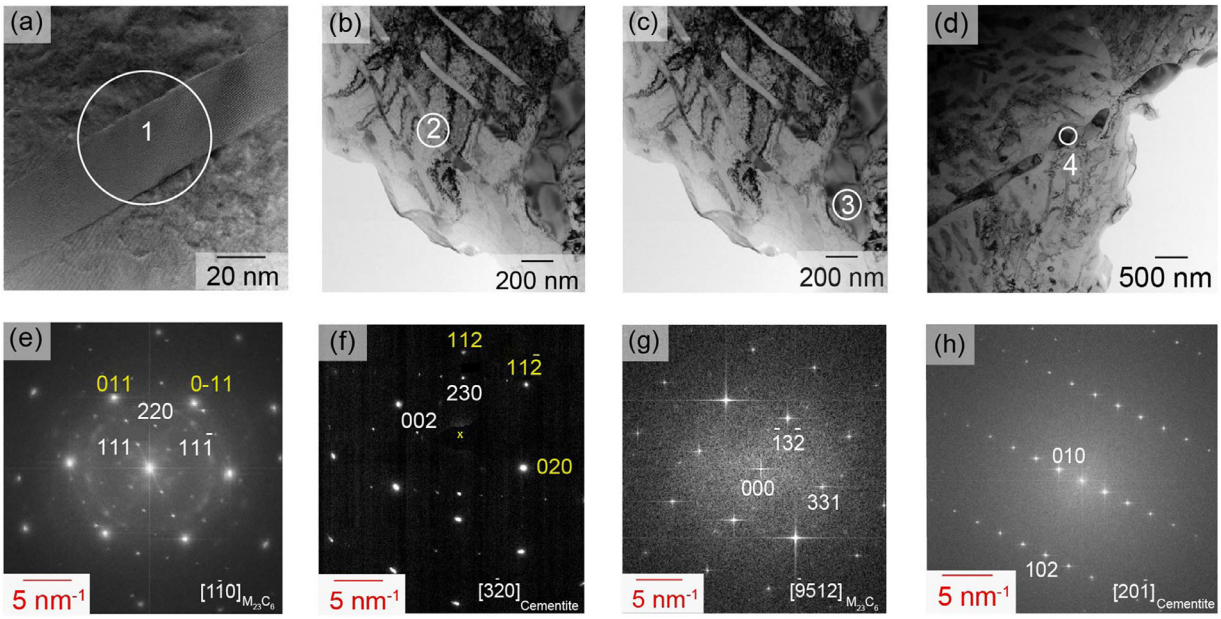

Fig. 5. TEM characterization of the carbides present in specimen z_{case}. (a) HRTEM and (b) bright field image of the pearlitic carbides, indicated as 1 and 2. The diffraction patterns collected from the encircled regions 1 and 2 are shown in (e) and (f), respectively. (c) and (d) show the bright field images, where 3 and 4 show the carbides at the prior austenite grain boundaries. The FFT of the HRTEM images taken from regions 3 and 4 are shown in (g) and (h).

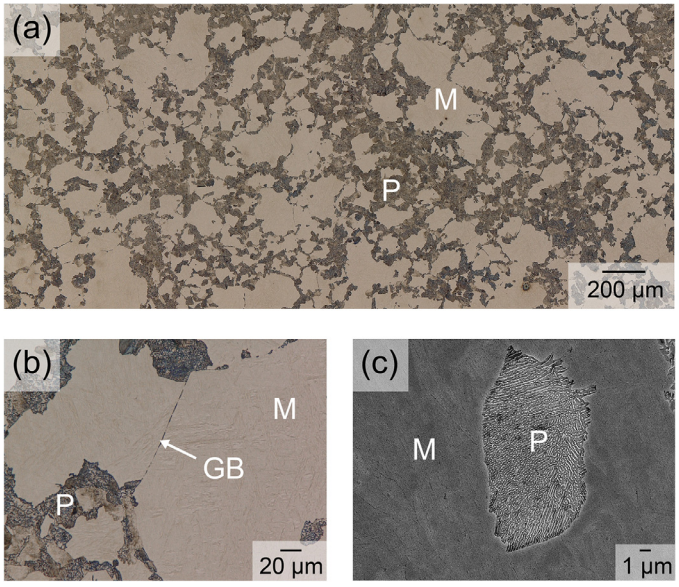

Fig. 6. (a, b) Optical and (c) scanning electron micrographs of specimen z_{tran} showing the various microstructural constituents. P: pearlite, M: martensite, and GB: γ/γ grain boundary.

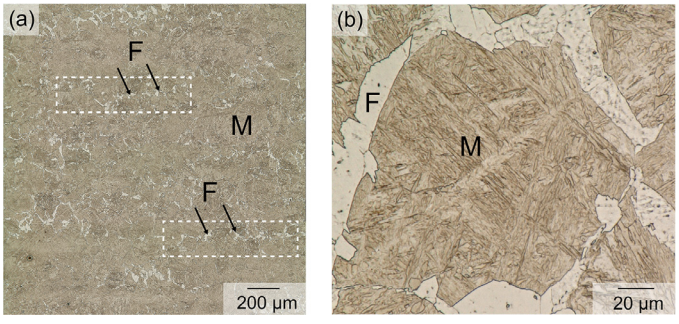

Fig. 7. (a) and (b) are the optical micrographs of specimen z_{core}. F: ferrite and M: martensite.

4. Discussion

4.1. Microstructure formation in the case region

Phase transformations preferentially begin at the prior austenite grain boundaries due to the grain boundary energy being annihilated during nucleation [20]. The observation of cementite and $M_{23}C_6$ (Fe-Cr-rich carbide according to equilibrium calculations) at the prior austenite grain boundaries in specimen z_{case} indicates that they are the primary products of austenite decomposition. These carbides are precipitated either during the cooling stage from the carburization treatment or during the isothermal treatment [21,22]. The thermodynamic possibility for the precipitation of carbides from austenite during the cooling stage is evaluated based on their driving force. The driving force for the formation of cementite and $M_{23}C_6$ from austenite is calculated separately from the property model of Thermo-Calc (TCFE10 database) and is shown as a function of temperature in Fig. 8. Driving force, represented on the *y*-axis in Fig. 8, is a non-dimensional parameter as it is normalized with $R \times T$, where R is the universal gas constant and T is the absolute temperature. A value higher than zero for driving force means that the nucleation of carbide is thermodynamically favorable. The simulation results show that cementite can precipitate at temperatures below ≈ 880 °C, while $M_{23}C_6$ can precipitate at temperatures below ≈ 840 °C. Cementite has a slightly higher driving force for nucleation than $M_{23}C_6$ up to 720 °C. As the temperature decreases continuously, the thermodynamic stability of both carbides increases, where below 720 °C, $M_{23}C_6$ emerges as the carbide with a higher driving force. These results show the thermodynamic possibility that cementite and $M_{23}C_6$ are both present at the prior austenite grain boundaries at the onset of isothermal holding at 600 °C.

Despite the positive driving forces, TC-PRISMA calculations indicate that the volume fractions of cementite and $M_{23}C_6$ are infinitesimally small at the start of isothermal holding. Therefore, the observable microstructural changes in specimen z_{case} are expected to occur during the isothermal treatment. In conventional steels, pearlite formation is due to the cooperative growth of α

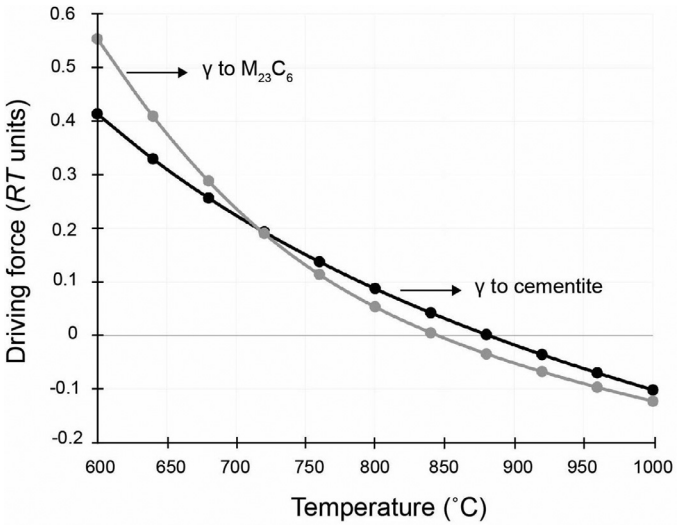

Fig. 8. Normalized driving force for the nucleation of cementite and $M_{23}C_6$ from austenite as a function of temperature for specimen z_{case}.

and cementite. In addition to α and cementite, γ and $M_{23}C_6$ are also stable phases at 600 °C in specimen z_{case} (see Fig. 4(a)). This implies that γ, α, cementite, and $M_{23}C_6$ coexist in equilibrium at the isothermal pearlitic treatment temperature. From a thermodynamic point of view, it is, therefore, possible for γ to decompose by two separate eutectoid reactions; (a) γ into α + cementite, and (b) γ into α + $M_{23}C_6$, forming two different pearlitic aggregates. This argument is supported by the TEM results (see Fig. 5) which show that both cementite and $M_{23}C_6$ are present as pearlitic carbides in specimen z_{case}.

A mixture of cementite and $M_{23}C_6$ as pearlitic carbides were previously reported by Cheng et al. in high Mn-Al steel [23,24]. However, in those studies, the volume fractions of the two carbides were not quantified due to the weak carbide signals in the XRD analysis. In the present study, the volume fractions of the carbides are quantifiable due to an almost complete isothermal austenite decomposition, unlike in Refs. [23,24]. The measured volume fractions of $M_{23}C_6$ and cementite differ from their equilibrium values by a factor of eight and two, respectively (see Fig. 4(a)). This high deviation in the carbide fractions can be rationalized by evaluating the activation energy for nucleation (ΔG^*). The activation energy for nucleation according to the classical nucleation theory can be written as [25]:

$$\Delta G^* = \psi / \Delta g_v^2 \quad (1)$$

where ψ is a factor that contains information about the shape of the nucleus and interfacial energy (σ_i), and Δg_v is the driving force for nucleation.

The driving force for nucleation (Δg_v) is a thermodynamic quantity that can be readily calculated from Thermo-Calc. The calculated values of Δg_v for the nucleation of $M_{23}C_6$, cementite, and α from γ at 600 °C are 0.55 *RT* units, 0.41 *RT* units, and 0.04 *RT* units, respectively. A positive value of Δg_v shows that their nucleation is thermodynamically possible. $M_{23}C_6$ has a higher driving force than cementite, which suggests that $M_{23}C_6$ has a higher nucleation potential (see also Fig. 8).

Additional parameters that influence the activation energy for nucleation are the interface energies (σ_i), which are contained in the term ψ of Eq. (1). Interfacial energy values are difficult to determine experimentally and are mostly deduced as a model fit parameter [26,27]. A first approximation of the interfacial energy values of the matrix and carbide phases is obtained using the property model calculator in Thermo-Calc with the TCFE10 database. The calculations in the approximation model are based on Becker's bond energy approach [28]. The interfacial energy of α and $M_{23}C_6$ ($\sigma_i^{\alpha/M23C6}$) is 0.15 J/m^2, while that for α and cementite ($\sigma_i^{\alpha/\theta}$) is 0.20 J/m^2. The calculated values of $\sigma_i^{\alpha/M23C6}$ and $\sigma_i^{\alpha/\theta}$ are in close agreement with the values reported in the literature for a similar temperature range; 0.1 J/m^2 for $\sigma_i^{\alpha/M23C6}$ [29] and 0.24 J/m^2 for $\sigma_i^{\alpha/\theta}$ [30].

The formation of pearlitic carbides also involves the interfacial energy contributions from the γ/α and γ/carbide interfaces. The γ/α interfaces are coherent or semi-coherent and are likely not rate-determining for pearlite nucleation [25]. However, the interfacial energy contribution of γ/carbide interfaces strongly affects the nucleation rate of the carbides, depending on their crystal structure and chemical composition [31]. The calculated interfacial energy values for $\gamma/M_{23}C_6$ and γ/θ interfaces are 0.06 J/m^2 and 0.07 J/m^2, respectively. These values differ significantly from that reported by Schneider et al. [32], which is 0.4 J/m^2. However, in Ref. [32], the interfacial energy value was a postulation based on the assumption that the carbides represent incoherent precipitates, for which σ_i is typically higher than 0.3 J/m^2 [26]. A clear basis for the selection of γ/carbide interfacial energy was not stated in [32]. From the experimental data on $M_{23}C_6$ size distribution and mean radius, Xiong et al. [27] obtained an interfacial energy of 0.024 J/m^2, which is close in agreement with the value reported in this study (0.06 J/m^2). The quantitative values of the interface energy calculation, therefore, provide a good approximation to the transformation event and point in the direction that the nucleation of $M_{23}C_6$ has a kinetic advantage over cementite.

These calculations show that the contribution of interfacial energy and driving force to the nucleation barrier for $M_{23}C_6$ and cementite are different. The calculated values show that the nucleation barrier for $M_{23}C_6$ is synergetically reduced by its higher driving force and lower interfacial energy compared to cementite. The faster nucleation kinetics of $M_{23}C_6$ results in a significantly higher volume fraction than cementite.

4.2. Microstructure formation in the transition region

The austenite decomposition products in specimen z_{tran} are pearlite and martensite, as shown in Fig. 6. Pearlite formed in this specimen is not preceded by the formation of pro-eutectoid products at the prior austenite grain boundaries. The absence of pro-eutectoid phases (ferrite or cementite) is usually associated with the austenite transformation into pearlite within a range of carbon composition close to the eutectoid carbon content of the steel [33]. The possible absence of pro-eutectoid phases in specimen z_{tran} is investigated by plotting the isopleth phase diagram, which is shown in Fig. 9. Fig. 9 shows that γ is a stable phase in all ranges of the plotted temperatures and carbon compositions. The eutectoid composition of the alloy is observed at 0.28 wt.% C, as indicated by the vertical dashed line, which is very close to the carbon content in specimen z_{tran} (0.3 wt.%). This is a very modest deviation and falls well inside the experimental and simulation uncertainties. Therefore, the absence of pro-eutectoid products in specimen z_{tran} is ascribed to its nearly eutectoid alloy composition.

The pearlitic microstructure of specimen z_{tran} is a mixture of α and $M_{23}C_6$. The presence of cementite as a microstructural constituent was not experimentally detected, unlike in specimen z_{case}. However, the phase equilibrium calculations give cementite as a stable phase at 600 °C along with α, $M_{23}C_6$, and γ (see Fig. 9). The volume fractions of these phases are shown in Table 2. The thermodynamic driving forces for the formation of various phases from γ at 600 °C and their interfacial energies are calculated using the property model in Thermo-Calc with the TCFE10 database. It can be noted from Table 2 that the driving force for the formation of $M_{23}C_6$ is higher than for cementite by a factor of three.

Table 2
Equilibrium fraction of the phases at 600 °C, driving force for nucleation, and interfacial energies in specimen z_{tran}.

Volume fraction of phases (vol.%)				Driving force (Δg_v) (RT units)			Interfacial energy (σ_i) (J/m^2)	
α	θ	$M_{23}C_6$	γ	γ to α	γ to θ	γ to $M_{23}C_6$	$\sigma i^{\alpha/\theta}$	$\sigma i^{\alpha}/M_{23}C_6$
92	3	2	3	0.08	0.12	0.38	0.24	0.21

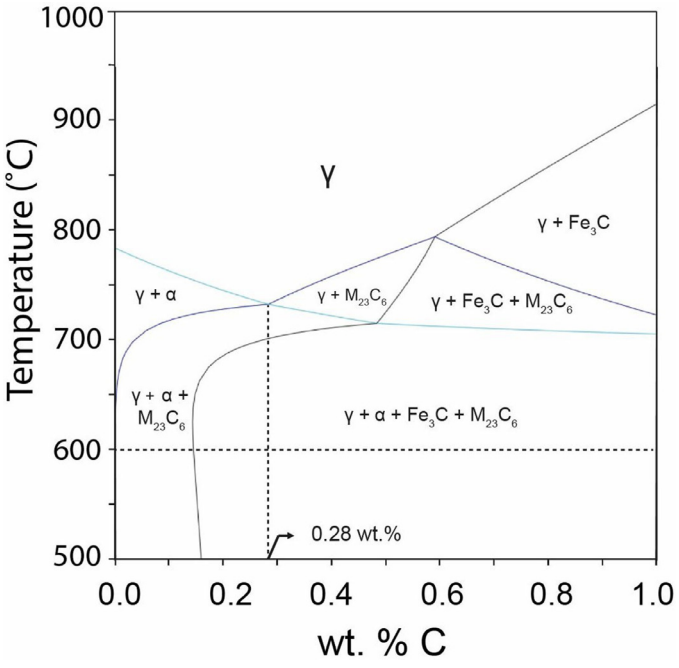

Fig. 9. Fe-C-3.3Ni-1.4Cr-0.55Mn-0.3Si-0.2Mo (wt.%) isopleth phase diagram.

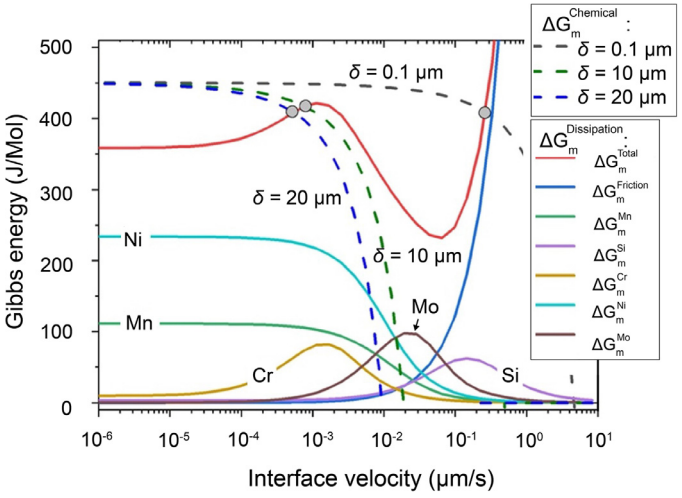

Fig. 10. Energy dissipation and chemical driving force versus interface velocity at different widths of ferrite layer (δ) for the case of isothermal austenite to ferrite phase transformation at T = 600 °C calculated by the GEB model in the Fe-0.16C-0.55Mn-0.4Si-1.4Cr-3.3Ni-0.2Mo (in wt.%).

Additionally, $M_{23}C_6$ has a lower interfacial energy value than cementite. This implies that the formation of pearlite favors the precipitation of $M_{23}C_6$. However, the calculations shown in Table 2 do not explain a complete absence/experimentally undetectable volume fraction of cementite in specimen z_{tran}, as cementite has a positive driving force for the formation and the calculated interfacial energy value with α is similar to that of $M_{23}C_6$. Therefore, it is likely that the kinetics of cementite formation has a more dominant influence. However, there is no experimental evidence in the present study that describes the associated governing mechanisms delaying or inhibiting cementite formation.

In contrast to an almost complete austenite decomposition in the span of 20 h at 600 °C for specimen z_{case}, only 40% of austenite transforms to pearlite in specimen z_{tran} (Fig. 6). This is a clear indication of the remarkable influence of carbon, concomitantly with the other alloying elements, on the pearlite formation kinetics. These observations are consistent with the results from an earlier study on a case-carburized Cr-Mo steel, where Nakajima et al. [34] reported an acceleration in the pearlite transformation with increasing carbon content due to pro-eutectoid carbide, which is a more effective nucleation site than pro-eutectoid ferrite.

4.3. Microstructure formation in the core region

The microstructure of specimen z_{core} is predominantly martensite with ferrite (6% to 7%) at the austenite grain boundaries, as shown in Section 3.2.3. The fraction of ferrite is much lower than the equilibrium ferrite fraction at 600 °C, which is 94% as simulated by the Thermo-Calc software. This significant difference between the experimentally observed and equilibrium fractions of ferrite can be explained by considering the solute drag effect of substitutional alloying elements on the migration rate of the γ/α interface. The general mixed-mode Gibbs energy balance (GEB) model [16] is applied to simulate the isothermal austenite to ferrite phase transformation at 600 °C. In the GEB model, the interface velocity is calculated by balancing the molar chemical driving force for phase transformation (ΔG_m) and the total energy dissipation caused by interfacial segregation of each substitutional alloying element (ΔG^i_m), i = Mn, Si, Cr, Ni, Mo, as well as the limited interface mobility, caused by the so-called interface friction (ΔG^f_m) [35]. The GEB model considers the effect of ferrite width (formed along γ/γ grain boundaries) on carbon redistribution ahead of the γ/α interface [36] and can explain the stasis in the ferrite formation with respect to changes in the available chemical driving force for the transformation. The details on the calculation of chemical driving force, dissipation of Gibbs energy, and consequently interface velocity with respect to ferrite width are extensively described in Ref. [16].

The observed ferrite in the microstructure is mainly grain-boundary ferrite with limited thickness between 10 and 20 μm after 20 h of isothermal holding at 600 °C (Fig. 7). In Fig. 10, the calculated energy dissipation is plotted together with the available chemical driving force at different widths (δ) of the ferrite layer (and consequently different compositions ahead of the α/γ interface) for the isothermal austenite to ferrite transformation at 600 °C in specimen z_{core}. In this graph, the intersection point between the curves of the chemical driving force and total dissipation specifies the actual interface velocity (v). The binding energies of the elements at the interface (E_0) for these calculations are set to E_0^{Mn} = 5 kJ/mol [37], E_0^{Si} = 12.3 kJ/mol [38], E_0^{Ni} = 5 kJ/mol [35], and E_0^{Mo} = 30.3 kJ/mol [39]. The binding energy of Cr is fitted as E_0^{Cr} = 9 kJ/mol since this parameter is not available in the literature for this model [40]. When the width of the ferrite is very low, δ = 0.1 μm (the degree of transformation is very small), the intersection point between the total dissipation and chemical driving force curves occurs at v = 0.15 μm/s. Under these conditions, there is minor dissipation of Gibbs energy by diffusion of substitutional

elements inside the moving interface, and the interface velocity is limited mainly by the interface mobility (ΔG^{f}_{m}) and carbon diffusion. With increasing width of the ferrite layer to $\delta = 10$ μm or 20 μm, the available chemical driving force decreases, and the curve of chemical driving force intersects the curve of total dissipation at much lower values of interface velocity (below 0.001 μm/s). At these very low interface velocities, the energy dissipation at the transformation interface by interfacial diffusion of substitutional alloying elements is relatively high, which indicates the segregation of these elements to the interface. For more hypothetical values of ferrite width ($\delta > 20$ μm), a much lower chemical driving force is available, and consequently, the growth rate continuously decreases to extremely low values ($v \ll 10^{-4}$ μm/s) as it is controlled by the bulk diffusion of the substitutional alloying elements in austenite, and the transformation reaches a stasis.

The GEB model predicts a velocity that can cause a physically realizable migration of interface ($v = 0.001$–0.1 μm/s) only for a very low ferrite width ($\delta < 10$ μm). This prediction is without considering the effect of the ferrite nucleation rate on the overall kinetics of isothermal ferrite formation. The regions of the ferrite phase observed in the final microstructure (Fig. 7) formed at different times of isothermal holding at 600 °C. The predictions by the GEB model are based on the solute drag effect of the substitutional alloying elements on the austenite/ferrite interface and are consistent with the observed ferrite width when the ferrite grain nucleated at the austenite grain boundaries grows into both neighboring austenite grains.

5. Conclusions

This work presents the influence of carbon concentration ranges arising from case carburization on the microstructures obtained after 20 h of isothermal treatment at 600 °C. The applied heat treatment results in a microstructure that is pearlitic in the high-carbon regions (case) and predominantly martensitic in the low-carbon areas (core). The case and core regions are separated by a sharp transition zone, where the microstructure is a mixture of pearlite and martensite. From microstructural analyses of specimens z_{case}, z_{tran}, and z_{core} of carbon compositions 0.9 wt.%, 0.3 wt.%, and 0.16 wt.%, respectively, the following conclusions are drawn:

(1) The formation of pearlite in the case (z_{case}) is preceded by the precipitation of two pro-eutectoid carbides at the prior austenite grain boundaries, cementite and $M_{23}C_6$. The final microstructure shows the co-existence of two different pearlite aggregates: ferrite + cementite and ferrite + $M_{23}C_6$. The pearlitic aggregate with $M_{23}C_6$ carbides has faster nucleation kinetics due to its lower interfacial energy with ferrite, and higher driving force for formation, compared to cementite.

(2) A clear transition in the case to core microstructures is observed at the eutectoid composition of the alloy, which corresponds to the carbon composition in specimen z_{tran} (0.3 wt.% C). The microstructure in the transition region is 60% martensite and 40% pearlite. The pearlitic carbide in this region is $M_{23}C_6$. Although cementite precipitation is not experimentally detected using XRD analysis, an assertion of its complete absence cannot be made from the present study. An experimentally undetectable volume fraction of cementite is surmised from the equilibrium phase predictions, in which case the competitive nucleation and growth of cementite and $M_{23}C_6$ favors the precipitation of the latter.

(3) The kinetics of pearlite formation slows down with the carbon concentration up to the eutectoid composition of the steel. Below the eutectoid composition, the pro-eutectoid ferrite formed during cooling results in the redistribution of the alloying elements at the γ/α boundary. This alloy redistribution exerts a solute-drag effect which significantly reduces the γ/α interface migration rate to such an extent that it limits the fraction of ferrite to well below the equilibrium fraction.

Declaration of Competing Interest

The authors declare that they have no known competing financial interests or personal relationships that could have appeared to influence the work reported in this paper.

Acknowledgments

The authors gratefully acknowledge the grant provided by Siemens Gamesa Renewable Energy (Denmark), SKF Research and Technology Development (The Netherlands), and the Dutch government through Top consortium for Knowledge and Innovation (TKI). The industrial partners of this project, Siemens Gamesa Renewable Energy (Denmark) and SKF Research and Technology Development (The Netherlands) are acknowledged for the materials and financial support. The authors would like to thank Mr. Ruud Hendrikx and Drs. Richard Huizenga at the Department of Materials Science and Engineering of the Delft University of Technology for the X-ray analysis, and Ing. C. Kwakernaak for performing EPMA measurements. The authors are also grateful to Dr. Ir. F.D. Tichelaar, Kavli Institute of Nanoscience, Delft University of Technology for the support with TEM imaging. The authors extend their gratitude to Dr. Ir. S.E. Offerman and Dr. Arthur Nishikawa for the fruitful discussions in the course of this work.

References

[1] G. Parrish, Carburizing: Microstructures and Properties, ASM International, 1999.
[2] R. Errichello, R. Budny, R. Eckert, Tribol. Trans. 56 (2013) 1069–1076.
[3] H. Bhadeshia, Prog. Mater. Sci. 57 (2012) 268–435.
[4] H. Schlicht, E. Schreiber, O. Zwirlein, Effect of Steel Manufacturing Processes On the Quality of Bearing Steels, ASTM International, 1988.
[5] H. Farivar, D. Novokshanov, S. Richter, D. Lenz, W. Bleck, U. Prahl, Mater. Sci. Eng. A 762 (2019) 138040.
[6] J.W. Morris Jr, ISIJ Int. 48 (2008) 1063–1070.
[7] T. Furuhara, K. Kikumoto, H. Saito, T. Sekine, T. Ogawa, S. Morito, T. Maki, ISIJ Int. 48 (2008) 1038–1045.
[8] M. Paladugu, R.S. Hyde, Wear 406 (2018) 84–91.
[9] E. Santos, K. Kida, T. Honda, H. Koike, J. Rozwadowska, Mater. Sci. 47 (2012) 677–682.
[10] Z. Cao, Z. Shi, F. Yu, K.-i. Sugimoto, W. Cao, Y. Weng, Int. J. Fatigue 128 (2019) 105176.
[11] K. Lee, S. Hong, Y. Kang, H. Yoon, S. Kang, Int. J. Automot. Technol. 10 (2009) 697.
[12] R. Saito, N. Nakada, S. Yabu, K. Hayashi, Metall. Mater. Trans. A-Phys. Metall. Mater. Sci. 49 (2018) 6001–6009.
[13] J.A. Mathews, J. Sietsma, R. Petrov, M. Santofimia, Mate. Des. (2022) 111232.
[14] F.C. Cerda, I. Sabirov, C. Goulas, J. Sietsma, A. Monsalve, R. Petrov, Mater. Des. 116 (2017) 448–460.
[15] V.A. Esin, B. Denand, Q.Le Bihan, M. Dehmas, J. Teixeira, G. Geandier, S. Denis, T. Sourmail, E. Aeby-Gautier, Acta Mater. 80 (2014) 118–131.
[16] H. Chen, S. Van Der Zwaag, Acta Mater. 72 (2014) 1–12.
[17] J. Armstrong, K. Heinrich, D. Newbury, in: Electron Probe Quantitation, Plenum Press, New York, 1991, pp. 261–316.
[18] M. Li, Gear Technol. (2016) 56–61.
[19] K. Andrews, J. Iron Steel Inst. (1965) 721–727.
[20] C. Zheng, N. Xiao, L. Hao, D. Li, Y. Li, Acta Mater. 57 (2009) 2956–2968.
[21] C.-Y. Hung, G. Spanos, R. Rosenberg, M. Kral, Acta Mater. 50 (2002) 3781–3788.
[22] M. Kral, G. Spanos, Scr. Mater. 36 (1997) 875–882.
[23] W.-C. Cheng, Y.-C. Li, Metall. Mater. Trans. A-Phys. Metall. Mater. Sci. 43 (2012) 1817–1825.
[24] W.-C. Cheng, S.-M. Hwang, Metall. Mater. Trans. A-Phys. Metall. Mater. Sci. 42 (2011) 1760–1766.
[25] S. Offerman, L. Van Wilderen, N. Van Dijk, J. Sietsma, M.T. Rekveldt, S. Van der Zwaag, Acta Mater. 51 (2003) 3927–3938.
[26] O. Prat, J. Garcia, D. Rojas, C. Carrasco, A. Kaysser-Pyzalla, Mater. Sci. Eng. A 527 (2010) 5976–5983.
[27] Q. Xiong, J.D. Robson, L. Chang, J.W. Fellowes, M.C. Smith, J. Nucl. Mater. 508 (2018) 299–309.
[28] R. Becker, Ann. Phys.-Berlin 424 (1938) 128–140.
[29] J. Sanhueza, D. Rojas, O. Prat, J. Garcia, R. Espinoza, C. Montalba, M. Melendrez, Mater. Chem. Phys. 200 (2017) 342–353.

[30] P. Deb, M. Chaturvedi, Metallography 15 (1982) 341–354.
[31] G. Spanos, Metall. Transact. A 23 (1992) 171–181.
[32] A. Schneider, G. Inden, Acta Mater. 53 (2005) 519–531.
[33] H. Bhadeshia, R. Honeycombe, Steels: Microstructure and Properties, Butterworth-Heinemann, 2017.
[34] H.-O. Nakajima, T. Araki, Transact. Iron Steel Inst. Jpn. 7 (1967) 9–18.
[35] J. Zhu, H. Luo, Z. Yang, C. Zhang, S. Van der Zwaag, H. Chen, Acta Mater. 133 (2017) 258–268.
[36] H. Chen, S. van der Zwaag, J. Mater. Sci. 46 (2011) 1328–1336.
[37] H. Fang, S. van der Zwaag, N. van Dijk, Acta Mater. 212 (2021) 116897.
[38] H. Chen, K. Zhu, L. Zhao, S. van der Zwaag, Acta Mater. 61 (2013) 5458–5468.
[39] H. Farahani, W. Xu, S. van der Zwaag, Philos. Mag. Lett. 98 (2018) 161–171.
[40] S.H. Kim, J.H. Kim, J.H. Lee, D.-W. Suh, J.S. Lee, Metals Mater. Int. 28 (2022) 2059–2067.